

Extreme Superluminal Motion in the Curved Jet of PKS 1502+106

T. An^{1,2}, X.Y. Hong^{1,2}, T. Venturi³, D.R. Jiang^{1,2}, and W.H. Wang^{1,2}

¹ Shanghai Astronomical Observatory, Chinese Academy of Sciences, Shanghai 200030, China

² National Astronomical Observatories, Chinese Academy of Sciences, Beijing 100012, China

³ Istituto di Radioastronomia del CNR, Via Gobetti 101, 40129 Bologna, Italy

Received <date> / Accepted <date>

Abstract. In this paper we present a multifrequency and multiepoch study of PKS 1502+106 at radio frequencies. The analysis is based on an EVN (European VLBI Network) dataset at 5 GHz and archive VLBA (Very Long Baseline Array) datasets at 2.3, 8.3, 24.4 and 43.1 GHz over a period of 8 years. The source is characterized by a multi-component one-sided jet at all epochs. The high-resolution images at 5, 8.3, 24.4 and 43.1 GHz show a curved jet morphology in the source. The radio core brightness temperature approaches the equipartition limit. Superluminal motions of 37.3 ± 9.3 c , 22.0 ± 15.5 c , 10.5 ± 2.6 c and 27.9 ± 7.0 c are measured in four distinct components of the jet. Our analysis supports the idea that the relativistic jet in PKS 1502+106 is characterised by extreme beaming and that its radio properties are similar to those of γ -ray loud sources.

Key words. galaxies: jets – galaxies: quasars: general – galaxies: quasars: individual: PKS 1502+106

1. Introduction

One of the most significant observational results of extragalactic γ -ray active galactic nuclei (AGNs) is that all EGRET-identified objects are radio-loud sources (Mattox et al. 1997). Relativistic beaming in the jet is used to explain the EGRET identification in radio-loud AGNs. The EGRET-identified sources have on average much faster apparent superluminal motions than the general population of radio-loud sources (Jorstad et al. 2001). From a statistical analysis of ΔPA (position angle differences between parsec- and kiloparsec-scale structures) of EGRET-identified AGNs, Hong et al. (1998) concluded that γ -ray loud radio quasars typically show aligned morphologies on parsec and kiloparsec scales. It is still a matter of debate if the γ -ray emission in AGNs is related to higher beaming in these sources.

The radio-loud active galactic nucleus (AGN) PKS 1502+106 (4C 10.39, OR103), $z = 1.833$ (Fomalont et al. 2000), is a highly polarized quasar (Tabara & Inoue 1980). A high and variable degree of polarisation in the optical band is reported by Impey & Tapia (1988). It is known to be active and variable at radio, optical and X-ray wavelengths. In particular, the source exhibits intensity variations by a factor of $3 \sim 5$ on timescales from weeks to months in the radio band; it shows intensity variations in the optical band with m_ν ranging from 19.5 to

18.6, and in the X-ray band by a factor ≥ 2 at 1 keV (George et al. 1994 and references therein).

PKS 1502+106 exhibits a 'core-jet-lobe' structure at radio wavelengths. A Very Large Array (VLA) image at 1.64 GHz (Murphy, Browne & Perley 1993) shows that a continuous jet extends to the southeast and leads to a lobe located ~ 7 arcsecond from the core. Very Long Baseline Interferometry (VLBI) observations (Fey, Clegg & Fomalont 1996; Fomalont et al. 2000; Zensus et al. 2002) show a well-defined jet starting to the southeast and sharply bending to the east at a distance of 3–4 mas from the core.

Our interest in PKS 1502+106 is related to the misalignment of the pc- and kpc-scale radio structure in AGNs and its relation to the γ -ray emission. Fichtel et al. (1994) reported an EGRET flux density upper limit in PKS 1502+106 of 7×10^{-8} photons $\text{cm}^{-2} \text{ s}^{-1}$ from the Phase I results. However, the source was not detected in the following EGRET observations (Thompson et al. 1995; Hartman et al. 1999). To study the relation between the ΔPA and γ -ray emission, we observed a sample of γ -ray blazars with the EVN at 5 GHz in Nov. 1997, in which PKS 1502+106 was observed as a gamma-ray source candidate (Hong et al. 2004).

In the next section we present the EVN observation of PKS 1502+106 at 5 GHz, and the data reduction. The analysis of the 5 GHz EVN image is performed in Sect. 3, where we also re-analyzed five epochs of Very Long

Table 1. Logs of the observations

Epoch (1)	Freq (GHz) (2)	BW (MHz) (3)	Array and Available Telescopes ^a (4)	D_{uv}^b (km) (5)
1994.52	2.3	16	VLBA(All 10)	8600
	8.3	16	VLBA(All 10)	8600
1997.85	5.0	28	EVN(Ef Sh Jb Ht Mc Nt On Tr Ur Wb)	~10000
1998.11	2.3	32	VLBA(BR FD MK OV PT) GC KK	
			VLBA(BR FD HN KP LA NL OV PT SC) GC WF GN	5600
	8.3	32	VLBA(BR FD HN KP LA NL OV PT SC) GC WF GN	5600
2002.37	24.4	32	VLBA(BR FD HN KP LA MK NL OV SC)	8600
	43.1	32	VLBA(BR FD HN LA MK NL OV SC)	8600
2002.65	24.4	30	VLBA(All 10)	8600
	43.1	32	VLBA(BR FD HN KP LA MK NL OV PT)	6600
2002.99	24.4	64	VLBA(FD HN KP LA MK NL OV PT SC)	8600
	43.1	64	VLBA(FD HN KP LA MK NL OV PT SC)	8600

^a EVN telescope codes: Ef: Effelsberg, Sh: Shanghai, Ht: HartRAO, Jb: Jodrell, Mc: Medicina, Nt: Noto, On: Onsala, Tr: Torun, Ur: Urumqi, Wb: Westerbork Array; the VLBA observations at epoch 1998.11 are performed using subarrays made up of the VLBA antennas together with 4 geodetic antennas: GC (Fairbanks, AK USA), WF (Westford, MA USA), GN (Green Bank, WV USA) and KK (Kokee Park, HI USA);

^b the longest baseline of the array, in unit of kilometer.

Table 2. Parameters of the images

Figure (1)	Epoch (2)	Freq (GHz) (3)	Real Beam ^a Maj×Min(mas),P.A.(°) (4)	Restored Beam ^b Maj×Min(mas),P.A.(°) (5)	S_{Peak}^c (Jy/b) (6)	rms ^d (mJy/b) (7)	Contours (mJy/b) (8)
Fig.1a	1994.52	2.3	7.18×3.78, -1.67	7.18×3.78, 0	1.81	1.1	3.5×(-1,1,2,...,256)
Fig.1b	1998.11	2.3	5.94×4.54, 13.7	7.18×3.78, 0	1.23	0.9	2.8×(-1,1,2,...,256)
Fig.2a	1997.85	5.0	1.36×1.21, 64.7	1.25×1.25, 0	0.80	0.7	3.0×(-1,1,2,...,256)
Fig.2b	1994.52	8.3	1.95×1.03, -1.19	1.25×1.25, 0	1.37	0.9	2.8×(-1,1,2,...,256)
Fig.2c	1998.11	8.3	1.62×1.23, 16.7	1.25×1.25, 0	0.68	0.6	2.0×(-1,1,2,...,256)
Fig.3a	2002.37	24.4	0.64×0.28, -1.08	0.64×0.28, 0	1.26	0.8	2.1×(-1,1,2,...,256)
Fig.3b	2002.65	24.4	0.70×0.32, -3.77	0.64×0.28, 0	0.73	0.9	2.8×(-1,1,2,...,256)
Fig.3c	2002.99	24.4	0.76×0.28, -6.0	0.64×0.28, 0	0.95	1.0	3.0×(-1,1,2,...,128)
Fig.4a	2002.37	43.1	0.37×0.16, -3.35	0.37×0.16, 0	0.82	1.0	3.0×(-1,1,2,...,256)
Fig.4b	2002.65	43.1	0.66×0.24, -20.3	0.37×0.16, 0	0.50	1.2	3.7×(-1,1,2,...,128)
Fig.4c	2002.99	43.1	0.44×0.16, -6.41	0.37×0.16, 0	0.59	1.0	3.2×(-1,1,2,...,128)

^a the beam size directly measured from the visibilities (FWHM);

^b the restored beam shown in the images (FWHM);

^c the peak brightness in the image;

^d the off-source rms noise level in the images.

Baseline Array (VLBA) datasets at 2.3, 8.3, 24.4 and 43.1 GHz obtained from the public archive of Radio Reference Frame Database (RRFID) for a consistent study with our data. To investigate the relativistic beaming in this source, we estimate the core physical parameters and measure the jet proper motions in Sect. 4. Conclusions and summary are given in Sect. 5. $H_0 = 65 \text{ km s}^{-1}\text{Mpc}^{-1}$ and $q_0 = 0.5$ are used in this paper.

2. Observations and data processing

Table 1 summarizes the observations in order of time. The epoch and frequency of the observations are given in Cols. 1 and 2. Column 3 gives the bandwidth in each observation. Column 4 presents the array and available antennas.

We note that the observations at epoch 1998.11 were carried out with the VLBA and 4 geodetic antennas. The longest baseline of the array is given in Col. 5.

PKS 1502+106 was observed with the EVN at 5 GHz on 7 November 1997. The observation was carried out in snapshot mode, and PKS 1502+106 was observed with 4 scans, each 13 minutes long. The raw data bits were obtained with the MKIII VLBI recording system with an effective bandwidth of 28 MHz and correlated in Bonn at the Max-Planck-Institute für Radioastronomie MKIII correlator with 4 seconds integration time. The correlated data bits were calibrated and corrected for residual delay and rate using NRAO AIPS (Astronomical Image Processing System). Data post-processing, including editing, amplitude and phase self-calibration, and imaging were car-

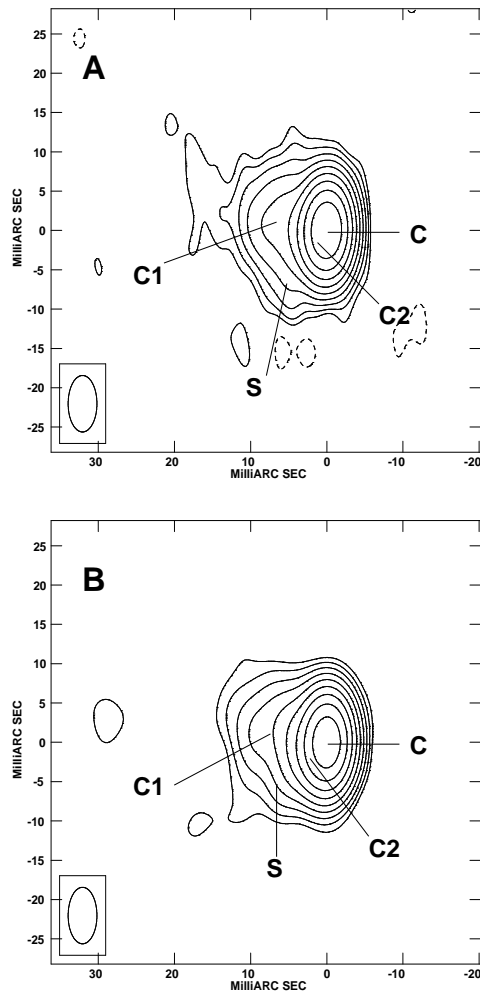


Fig. 1. VLBA images of PKS 1502+106 at 2.3 GHz. A: epoch 1994.52; B: epoch 1998.11.

ried out by means of the AIPS and DIFMAP packages (Shepherd, Pearson & Taylor 1994). The amplitude uncertainty is about 5% as estimated from the amplitude gain calibration. The task MODELFIT in the DIFMAP package was used in fitting models to the calibrated *uv* datasets.

The five epochs of dual-frequency VLBA archive datasets, observed from 1994 to 2002, were also re-imaged with natural weight and analyzed using AIPS and DIFMAP. Details of the observations are given in Table 1. The calibration errors of the VLBA datasets are mainly caused by receiver noise, and are estimated to be ~ 1 mJy/beam (Fey, Clegg & Fomalont 1996; Fomalont et al. 2000).

3. Analysis of the images

The images at 2.3, 5, 8.3, 24.4 and 43.1 GHz are shown in Figs. 1 to 4 in increasing order of frequency. They are all naturally weighted images. Each figure includes all epochs at the same frequency. As is clear from Table 2, the rms noise level ranges from 0.6 to 1.2 mJy beam $^{-1}$. The dy-

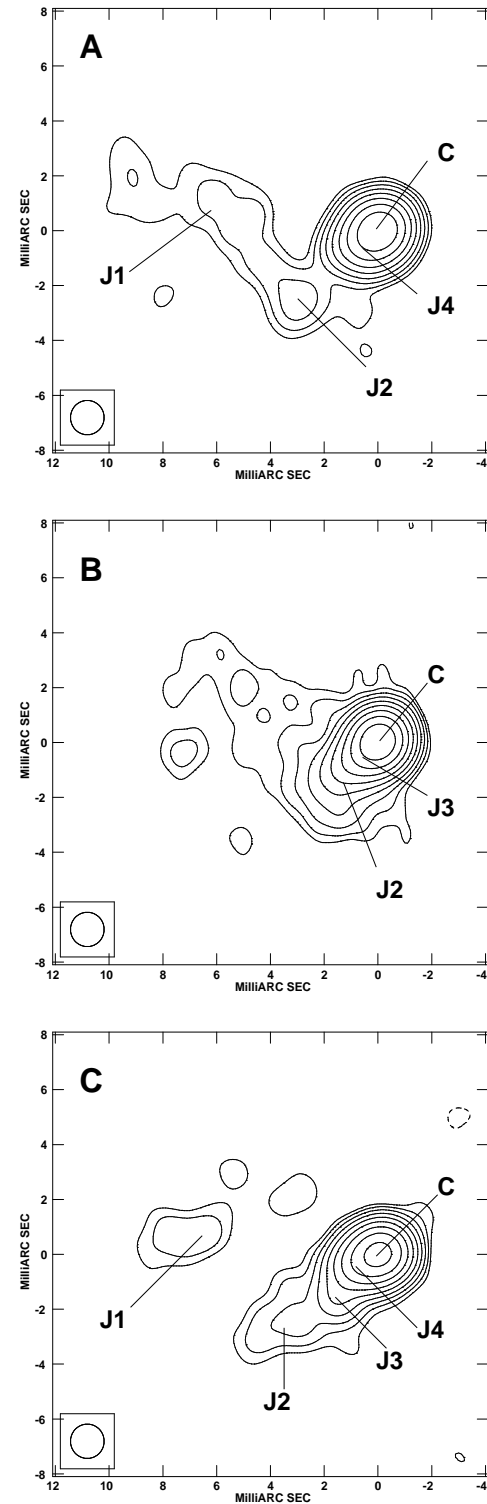


Fig. 2. VLBI images of PKS 1502+106. A: EVN image at 5 GHz at epoch 1997.85; B: VLBA image at 8.3 GHz at epoch 1994.52; C: VLBA image at 8.3 GHz at epoch 1998.11.

namic range (ratio of peak intensity to noise level) of the final images depends on the *uv* coverage and on the quality of the datasets. Except for the 2002.65 43.1 GHz dataset, whose *uv*-coverage is rather poor, in all images we obtain

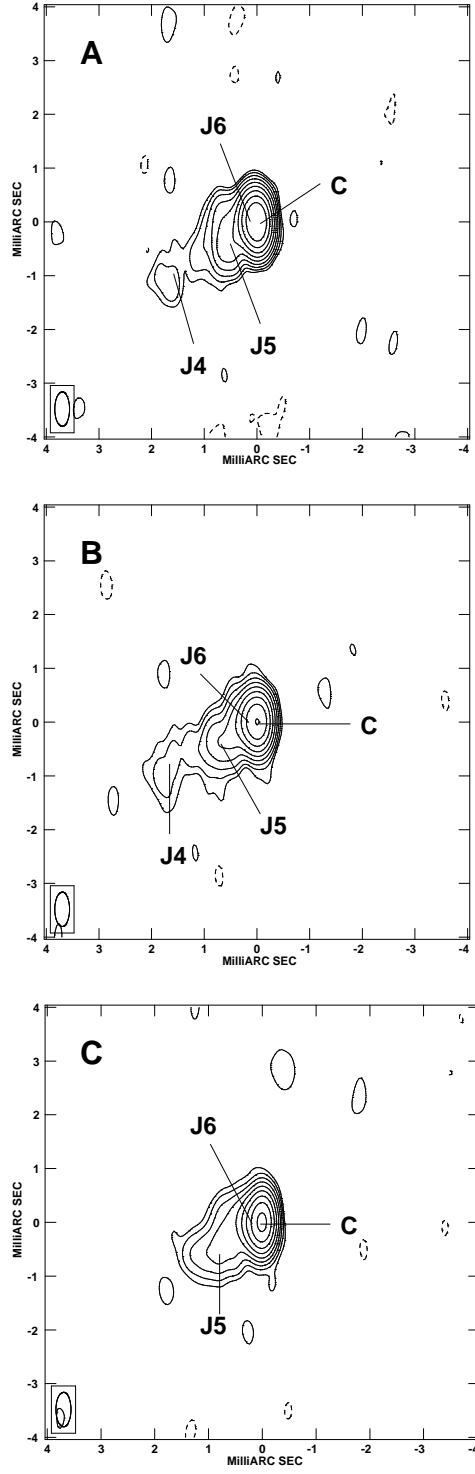


Fig. 3. VLBA images of PKS 1502+106 at 24.4 GHz. A: epoch 2002.37; B: epoch 2002.65; C: epoch 2002.99.

high dynamic ranges, between $\sim 850:1$ and $\sim 1700:1$. For a proper comparison, the datasets at 2.3 GHz were re-imaged with the same cellsize and restored with the same $\text{FWHM} = 7.18 \times 3.78 \text{ mas}$; the 5 GHz and 8.3 GHz datasets were restored with the same $\text{FWHM} = 1.25 \times 1.25 \text{ mas}$; the 24.4 and 43.2 GHz images were restored with a beam of $0.64 \times 0.28 \text{ mas}$ and $0.37 \times 0.16 \text{ mas}$, respectively. Detailed

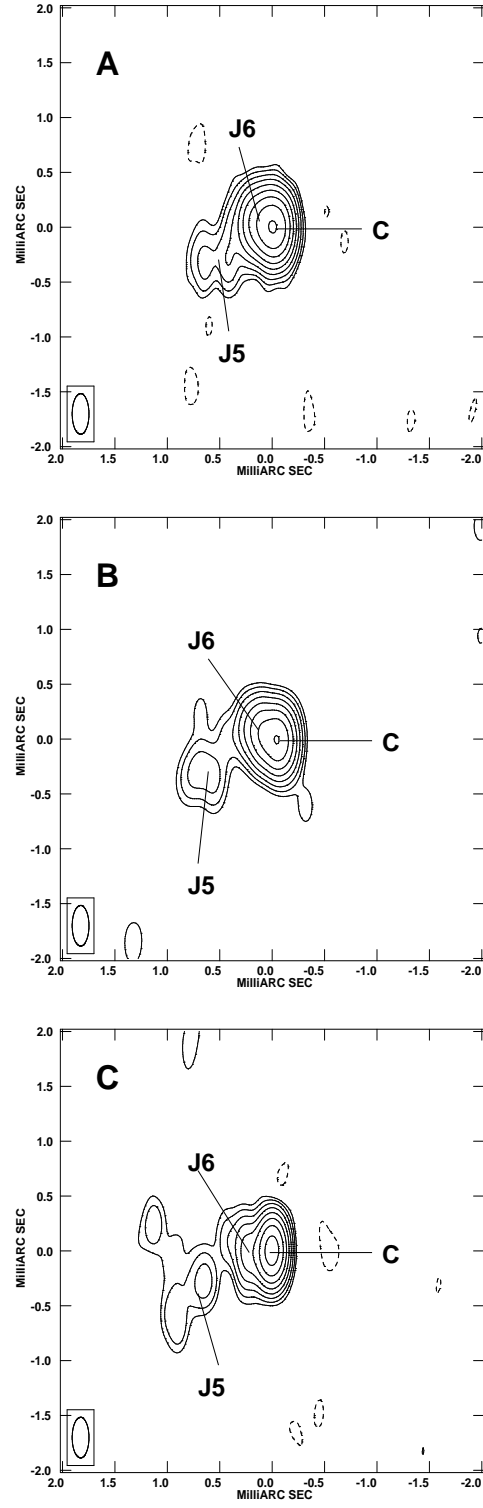


Fig. 4. VLBA images of PKS 1502+106 at 43.1 GHz. A: epoch 2002.37; B: epoch 2002.65; C: epoch 2002.99.

parameters of the images are given in Table 2 with the following format: Col. 1 lists the figure label of the image; cols. 2 and 3 provide the observing epoch and frequency; col. 4 gives the real beam which is directly obtained from the self-calibrated visibilities. Column 5 presents the re-

stored beam shown in each contour image. Columns 6 and 7 give the peak flux density and the off-source rms fluctuation in the image, respectively. The rms noise in each image is estimated in the final CLEANed images. Column 8 lists the contour levels in the images. The lowest contour level is generally about 3 times the rms noise level in the image.

3.1. The parsec-scale morphology

From the images in Figs. 1 to 4 it is clear that PKS 1502+106 is characterized by an asymmetric parsec-scale structure, with a dominant component and a one-sided jet. We note that images at different frequency and resolution highlight different features of the parsec-scale emission. The core region and the position angle of the jet change considerably over the resolution and frequency range studied here. Moreover, the images clearly show the morphological variability of the source with time.

In the 2.3 GHz images (Fig. 1) the jet points to the east of the core and extends up to ~ 15 mas. No counter-jet emission is detected in the images. The 5 and 8.3 GHz images in Fig. 2 reveal a curved jet structure within 8 mas. The inner jet moves out to the southeast of the core, then it turns sharply to the northeast at a distance of 3–4 mas. No emission brighter than $4 \times \text{rms}$ (i.e., 3 mJy/b in Fig. 2a) is detected beyond 10 mas east of the core. The three-epoch VLBA images at 24.4 GHz in Fig. 3 show the substructure of the jet in the inner 2 mas. The jet continuously extends to the southeast, and its position angle is in good agreement with the inner southeastern jet detected at 5 and 8.3 GHz. Fig. 3a (epoch 2002.37) and Fig. 3b (epoch 2002.65) show that the jet brightness decreases beyond 1 mas. The 43.1 GHz images in Fig. 4 make it possible to resolve the core region. The position angle of the jet within ~ 0.5 mas is $\sim 70^\circ$ at epoch 2002.37 and 2002.65 (Figs. 4a and 4b respectively), very different from the alignment beyond 1 mas, where the jet points towards the southeast. We also note the knotty appearance of the jet at epochs 2002.65 (Fig. 4b) and 2002.99 (Fig. 4c).

3.2. Analysis of the parsec-scale jet structure

Model fitting of the radio structure of each image was performed using the MODELFIT procedure of the Caltech DIFMAP software package. Table 2 contains the parameters of the major components for each dataset shown in Figs. 1 to 4. Column 1 lists the figure label. Columns 2 and 3 provide the epoch and frequency of the observation. Column 4 lists the component label. Component C, assumed to be the stationary core, is the strongest and most compact component in each image. Due to the different frequency and resolution, accurate identification of the components between 2.3 GHz and higher frequencies is impossible. To avoid possible frequency-dependent misidentifications, we labelled the jet components at 2.3 GHz as C1, C2 and S, and the jet components at 5, 8.3, 24.4 and

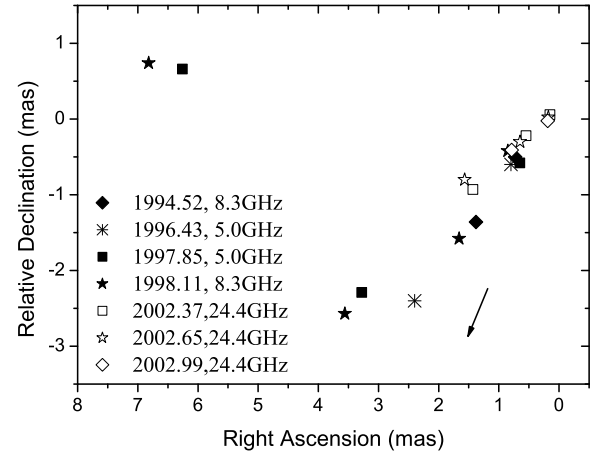


Fig. 5. Two-dimensional projected structure of the VLBI jet in PKS 1502+106. Symbols are as follows. *solid diamond*: epoch 1994.52, 8.3 GHz (this paper); *asterisk*: epoch 1996.43, 5 GHz (Fomalont et al. 2000); *solid square*: epoch 1997.85, 5 GHz (this paper); *solid star*: epoch 1998.11, 8.3 GHz (this paper); *open square*: epoch 2002.37, 24.4 GHz (this paper); *open star*: epoch 2002.65, 24.4 GHz (this paper); *open diamond*: epoch 2002.99, 24.4 GHz (this paper). The arrow indicates the P.A. of the lobe on the arc-second scale in the VLA image (Murphy, Browne & Perley 1993). To avoid confusion, the component error bars are not shown in the image.

43.1 GHz with J1 to J6 from the outermost region going inwards. Column 5 gives the total flux density of each component. Columns 6 and 7 list the separation and position angle of each component with respect to the core. Columns 8, 9 and 10 give the parameters of the Gaussian components: the major axis, the axis ratio and the orientation of the major axis. An elliptical Gaussian component is usually chosen to fit the core; however, in those cases where an axial ratio smaller than 0.1 was found, we carried out the fit using a circular Gaussian component. Circular Gaussians are used for the jet components to estimate their sizes. The overall uncertainty of the flux density in each dataset is the quadratic sum of the flux calibration error and the post-fitted rms error in the image. We present the flux density errors of discrete, bright components in each dataset. The errors in the component positions are proportional to the beam size from the formula given by Fomalont (1999). In model fitting, we noticed that on average the positions of the Gaussian components vary less than $\text{FWHM}/4$. For this reason we used $1/4$ of the beam major axis as the upper limit of the position error for most of the components.

At 2.3 GHz we fitted three bright components, labelled as C, C1 and C2 in Fig. 1. Furthermore, at both epochs we found a weak component (labelled S), located at 8–9 mas to the southeast of component C.

Table 3. Component parameters from the model fitting

Figure	epoch	Freq (GHz)	Comp	S (Jy)	R (mas)	θ (deg)	a (mas)	b/a	p.a. (deg)
(1)	(2)	(3)	(4)	(5)	(6)	(7)	(8)	(9)	(10)
Fig.1a	1994.52	2.3	C	1.650 \pm 0.276	0	0	0.97	0.21	-43
			C2	0.294	1.77 \pm 0.37	118.2	1.50	1	...
			C1	0.165	6.68 \pm 1.36	80.0	5.34	1	...
			S	0.023	8.75 \pm 0.32	137.2	1.45	1	...
Fig.1b	1998.11	2.3	C	1.231 \pm 0.160	0	0	1.38	0.70	-64
			C2	0.141	2.62 \pm 0.64	124.0	2.58	1	...
			C1	0.143	5.67 \pm 1.55	81.0	6.70	1	...
			S	0.010	9.19	131.0
Fig.2a	1997.85	5	C	0.874 \pm 0.165	0	0	0.69	0.66	-53
			J4	0.256	0.87 \pm 0.21	132.0	0.84	1	...
			J2	0.042	4.00 \pm 0.32	125.0	1.25	1	...
			J1	0.060	6.29 \pm 1.15	84.0	4.60	1	...
Fig.2b	1994.52	8.3	C	1.390 \pm 0.237	0	0	0.45	0.15	-42
			J3	0.218	0.89 \pm 0.13	124.5	0.50	1	...
			J2	0.170	1.94 \pm 0.40	134.5	1.61	1	...
			C	0.728 \pm 0.191	0	0	0.58	0.23	-72
Fig.2c	1998.11	8.3	J4	0.180	0.95 \pm 0.13	116.3	0.50	1	...
			J3	0.031	2.29 \pm 0.13	133.6	< 0.1	1	...
			J2	0.027	4.39 \pm 0.41	125.8	1.64	1	...
			J1	0.019	6.86 \pm 0.32	83.8	1.28	1	...
			C	1.030 \pm 0.166	0	0	0.08	1	...
Fig.3a	2002.37	24.4	J6	0.524 \pm 0.10	0.162 \pm 0.028	69.0	0.11	1	...
			J5	0.164	0.590 \pm 0.128	112.1	0.51	1	...
			J4	0.060	1.706 \pm 0.330	123.2	1.32	1	...
			C	0.645 \pm 0.115	0	0	0.13	1	...
Fig.3b	2002.65	24.4	J6	0.342	0.178 \pm 0.043	82.7	0.17	1	...
			J5	0.129	0.713 \pm 0.118	114.8	0.47	1	...
			J4	0.039	1.760 \pm 0.223	117.1	0.89	1	...
			C	0.870 \pm 0.160	0	0	0.05	1	...
Fig.3c	2002.99	24.4	J6	0.251	0.190 \pm 0.043	97.0	0.17	1	...
			J5	0.130	0.888 \pm 0.138	117.6	0.55	1	...
			C	1.050 \pm 0.194	0	0	0.15	0.44	85.3
			J6	0.348	0.165 \pm 0.040	72.2	0.16	1	...
Fig.4a	2002.37	43.1	J5	0.090	0.564 \pm 0.100	115.4	0.40	1	...
			C	0.611 \pm 0.197	0	0	0.14	1	...
			J6	0.294	0.186 \pm 0.043	68.4	0.17	1	...
			J5	0.081	0.770 \pm 0.088	112.0	0.35	1	...
Fig.4b	2002.65	43.1	C	0.645 \pm 0.252	0	0	0.07	1	...
			J6	0.107	0.211 \pm 0.035	93.7	0.14	1	...
			J5	0.051	0.750 \pm 0.065	114.0	0.26	1	...

The source morphology at 5 and 8.3 GHz is well described with four components along the jet, labelled J1 to J4. Component J3 is detected at 8.3 GHz at both epochs, but it does not appear at 5 GHz. We failed to fit the extended emission at 3–6 mas in Fig. 2b with a single gaussian component, due to its extent and low brightness. We note that component J1 is identified at 5 GHz, epoch 1997.85 (Fig. 2a) and at 8.3 GHz, epoch 1998.11 (Fig. 2c).

Two new components, J5 and J6, are fitted closer to the core at 24.4 and 43.1 GHz (Fig. 3 and 4). Component J5 is located at $\sim 0.5 - 1.0$ mas, southeast of the core. Component J6 is the closest to the core, at ~ 0.2 mas. We note the good agreement in the position angle of J5 and J6 at the two frequencies. Component J4 appears at the

end of the southeastern jet, ~ 1.7 mas, in P.A. $\sim 120^\circ$ (Fig. 3a and 3b).

Fig. 5 displays the projected position of the jet components in PKS 1502+106 at different epochs and frequencies in an RA–DEC diagram. The symbols represent the components at different frequencies. Fig. 6 shows the distribution of jet component position angles with radial distance from the core. Components J1 to J6 are shown with different symbols. The investigation of the motions for the individual jet components suggests a continuous, curved jet path. The jet starts at a P.A. $\sim 70^\circ$, and then changes to a P.A. $\sim 110^\circ$ in the inner 0.5 mas. Another sharp jet bending takes place at about 3–4 mas from the core, where the position angle changes from $\sim 130^\circ$ to

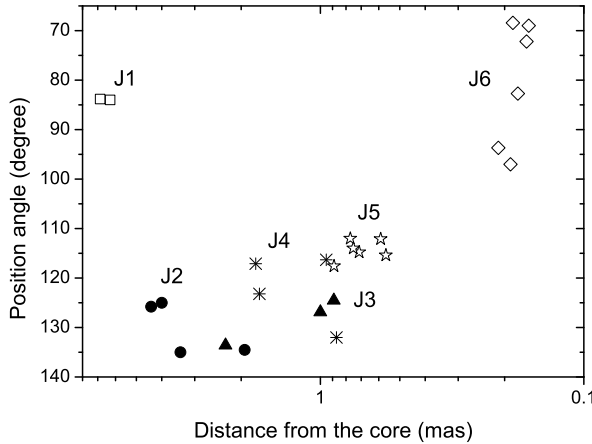


Fig. 6. The distribution of jet component position angles along the radial distance in PKS 1502+106. The x -axis shows the distance from the core on a logarithmic scale and y -axis shows the position angle, measured from north to east. Symbols are as follows: *open square* shows component J1, *solid circle* J2, *solid triangle* J3, *asterisk* J4, *open star* J5 and *open diamond* J6.

$\sim 80^\circ$. A helical pattern associated with hydrodynamical instabilities might explain the oscillations of the jet position angles (Hardee 1987).

3.3. Misalignment between the parsec and kiloparsec jet

To study the radio structure of PKS 1502+106 quantitatively, we examined the jet position angle on different scales. From the above analysis of the jet structure, the jet direction oscillates in the range 70° – 130° – 80° within the inner 8 mas. To have a reference position angle, we define the P.A. at 10 pc from the core as the value on the parsec scales (P.A._{pc}). At the distance of PKS 1502+106, 10 parsec corresponds to about 1.5 mas (the dashed line in Fig. 7 indicates the distance). We note that the position angle of the jet in the inner 3 mas changes with frequency (Fig. 7). In particular, the P.A. at high frequency is systematically lower than the P.A. at low frequency. The jet axis is directed to a P.A. of $\sim 115^\circ$ at 43.1 GHz, $\sim 120^\circ$ at 24.4 GHz and $\sim 130^\circ$ at 5 and 8.3 GHz. We believe that this slight discrepancy is due to opacity effects, and the measurement is frequency dependent. We assume a mean value of 125° as the P.A. on parsec scales. The kiloparsec-scale jet in PKS 1502+106, on the whole, leads to a south-east lobe along a continuously collimated path (Murphy, Browne & Perley 1993). The P.A. of the kiloparsec-scale jet (P.A._{kpc}) is measured along the direction connecting the peak and the lobe, and is $\sim 157^\circ$. Thus the difference of jet position angles measured on parsec and kiloparsec scales (ΔPA) is 32° .

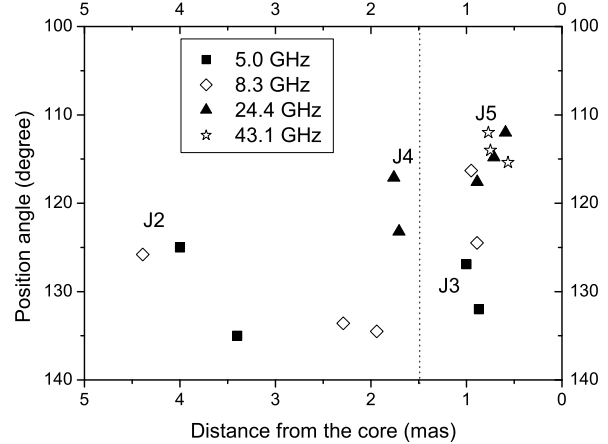


Fig. 7. The frequency-dependence of jet position angles on the parsec scale in PKS 1502+106. The x -axis and y -axis are defined as radial distance and position angle of the jet components, respectively. Symbols are as follows. *solid square* 5 GHz, *open diamond* 8.3 GHz, *solid triangle* 24.4 GHz, *open star* at 43.1 GHz. The dashed line represents the distance at which we measured P.A._{pc}.

Table 4. The spectral index of individual component on pc scales

Spectral index	C	J6	J5	J4	J2	J1	
$\alpha_{8.3}^{5}$ (1998.11)	-0.36				-0.70	-0.87	-2.27
$\alpha_{43.1}^{24.4}$ (2002.37)	0.03	-0.72	-1.05				
$\alpha_{43.1}^{24.4}$ (2002.65)	-0.09	-0.27	-0.87				
$\alpha_{43.1}^{24.4}$ (2002.99)	-0.52	-1.64	-1.50				

4. Physical parameters

4.1. The spectral index in the core region

Dual-frequency simultaneous VLBA observations allow us to estimate the spectral index distribution of the source ($S \propto \nu^\alpha$). We used the model fitting results in Table 3 to estimate the spectral index for the individual components. In particular, we used the two simultaneous datasets at 24.4 and 43.1 GHz to derive the spectral index of the core and the inner jet components J5 and J6. Furthermore, we also estimated the spectral index of components C, J1, J2 and J4 by comparing two non-simultaneous datasets, 1997.85 5 GHz data and 1998.11 8.3 GHz data. The results are listed in Table 4. As expected, the spectrum is flat in the core region, and steeper along the inner 4 mas jet. We note that the spectrum is systematically steeper at epoch 2002.99, and the flux density of each jet component decreases from epoch 2002.65 to epoch 2002.99 both at 24.4 and 43.1 GHz. This could be due to an expansion of the jet. The 5 GHz EVN data and 8.4 GHz VLBA data are not simultaneous and the *uv* coverage of the two arrays is also different, therefore the spectral index estimated between these two frequencies should be taken with caution. The

Table 5. Intrinsic Parameters and Doppler Factor in the radio core

Epoch	1997.85	1994.52	1998.11	2002.37	2002.65	2002.99	2002.37	2002.65	2002.99
Freq(GHz)	5	8.3	8.3	24.4	24.4	24.4	43.1	43.1	43.1
$T_b^{(a)} (10^{12} \text{K})$	0.38	2.30	0.47	0.93	0.22	2.02	0.20	0.06	0.24
δ_{eq}	1.87	15.0	2.45	5.20	0.99	13.0	0.91	0.21	1.14
$T_r^{(b)} (10^{12} \text{K})$	0.20	0.15	0.19	0.18	0.22	0.16	0.22	0.27	0.21

^(a) observed radio core brightness temperature;

^(b) intrinsic radio core brightness temperature, taking into account the Doppler boosting factor.

total flux density decreased by 21% from epoch 1997.85 to epoch 1998.11.

4.2. Equipartition Doppler factor and brightness Temperature

Assuming that the source is at or near equipartition of energy between radiating particles and magnetic field, we can estimate the equipartition Doppler factor δ_{eq} of the radio core (Readhead 1994 and Güijosa & Daly 1996) with the formula:

$$\delta_{eq} = [[10^3 F(\alpha)]^{34} \{[1 - (1+z)^{-1/2}]/2h\}^{-2} S_{op}^{16} \theta_d^{-34} \times (1+z)^{15-2\alpha} (\nu_{op} \times 10^3)^{-(2\alpha+35)}]^{1/(13-2\alpha)}, \quad (1)$$

where z is the redshift and θ_d is the angular diameter of the source. In computing the Doppler factors, we assumed an optically thin spherical index $\alpha = -0.75$ and a spherical geometry, as was used by Güijosa & Daly (1996). $h = 0.65$ is defined. For an elliptical gaussian component, θ_d is larger than the observed angular diameter θ_{FWHM} . Marscher (1987) suggested a correction for this by using $\theta_d = 1.8\theta_{FWHM}$. S_{op} is defined as the observed flux density at the self-absorption turnover frequency ν_{op} .

The equipartition method requires that observations are carried out at the self-absorption turnover frequency. However it is difficult to obtain the VLBI core parameters in PKS 1502+106 at the exact turnover frequency, since the core shows a flat spectrum between the observing frequencies from 2.3 to 43.1 GHz (Table 4). Assuming the VLBI observing frequency as the turnover frequency, we roughly estimate the Doppler boosting factor using the available VLBI core parameters. The formula for the equipartition Doppler factor is geometry dependent. The Doppler factor in a jet model is slightly larger than that in the spherical case for $\delta > 1$, $\delta_{eq}(\text{jet}) \propto \delta_{eq}^{1.4}(\text{sph})$. We note that the most compact component at lower frequencies is resolved into a compact component and initial jet at higher frequencies. Particularly, the core component at 2.3 GHz includes the core and the southeast innermost jet portion. So we limited the estimates of the Doppler factors to the data of the most compact component C at 5, 8.3, 24.4 and 43.1 GHz to minimize the geometry-dependence uncertainty. The estimated δ_{eq} values are listed in Table 1. We assume a mean value $\delta = 4.5 \pm 1.9$ as the best estimate of the Doppler boosting factor in the core of PKS

1502+106. In practice, a low limit to δ_{eq} in PKS 1502+106 has been calculated with an assumed optically thin spectral index ($\alpha = -0.75$) in the formula (Readhead 1994).

The brightness temperature T_b of a Gaussian component in the source rest frame is given by Shen et al. (1997):

$$T_b = 1.22 \times 10^{12} \frac{S_{op}}{\nu_{op}^2 ab} (1+z) \text{ K}, \quad (2)$$

where a and b are the major and minor axes in unit of mas, other parameters are defined same as Eq. (1). The radio core flux density and dimensions are taken from Table 3. Taking into account the Doppler boosting factor, we get the equivalent value of the intrinsic brightness temperature T_r ($T_r = T_b/\delta$). The estimated values of T_b and T_r are presented in Table 5 and we assume a mean value $T_r = (2.0 \pm 0.5) \times 10^{11} \text{K}$ as the best estimate of the intrinsic brightness temperature in the source frame. The major errors of T_r are introduced by the fitted core size and the source variation. Due to the resolution limit, we only obtain the lower limit of the brightness temperature. Readhead (1994) suggested that the equipartition temperature is likely to be $10^{10} \sim 10^{11} \text{K}$ in most sources. We can see that the intrinsic radio core brightness temperature in the source, $(2.0 \pm 0.5) \times 10^{11} \text{K}$, approaches the equipartition limit.

4.3. Superluminal motion in the parsec-scale jet

In the discussion of the parsec-scale jet structure (Section 3.2), we suggested that the jet components in PKS 1502+106 follow the same curved trajectory. For component J6 we find only a marginal indication of radial motion, however we note that its position angle changes significantly at the same radial distance from the core. The extended component J1 is detected only in two epochs, therefore its proper motion is estimated with a large uncertainty. For these reasons, we only calculate and discuss the proper motion for the well-defined components J2, J3, J4 and J5. The time evolution of the position of each component with respect to the (assumed) stationary core is reported in Fig. 8. We underline that due to possible opacity effects and frequency-dependent offsets in the position, only the Gaussian components at the three frequencies 5, 8.3 and 24.4 GHz are considered in the study of the motion. We also include the 5 GHz Gaussian models presented by Fomalont et al. (2000) for a more complete analysis (see caption to Fig. 8).

Table 6. Proper motion of jet components in PKS 1502+106

Comp	μ (mas/yr)	β_{app}
J2	0.64 ± 0.16	$37.3 \pm 9.3 c$
J3	0.38 ± 0.26	$22.0 \pm 15.5 c$
J4	0.18 ± 0.04	$10.5 \pm 2.6 c$
J5	0.48 ± 0.12	$27.9 \pm 7.0 c$

We performed least-squares fits to the component distances from the cores as a function of time. To minimize the effects of frequency-dependent separation we took the model fitting errors as the statistical weight and measured the overall weighted mean velocities. The results are presented in Table 6, where μ represents the proper motion and β_{app} denotes the apparent velocity. The measured proper motions range between 0.18 ± 0.04 and 0.64 ± 0.16 mas/yr, corresponding to apparent velocities in the range between $10.5 \pm 2.6 c$ and $37.3 \pm 9.3 c$. These estimated speeds are significantly higher than the average superluminal speed of jet components in radio loud quasars (Pearson et al. 1998). Jorstad et al. (2001) found that the mean apparent velocities of γ -ray quasars increase with redshift. The average velocity for high redshift ($2 \leq z \leq 2.5$) quasars is $15.9 \pm 6.6 h^{-1}c$ (i.e., $24.5 \pm 10.2 c$ for $h = 0.65$). Except for the highest superluminal velocity, $37.3 \pm 9.3 c$, the apparent speeds in PKS 1502+106 ($z = 1.833$) are in good agreement with the statistical mean value of Jorstad et al. (2001).

We note that the highest speed is associated with the jet component J2, located at the position of the jet bending, i.e. 3–4 mas from the peak. A possible explanation for the very high speed of J2 is that its observed properties are magnified by projection effects. We note that at the very high levels of beaming revealed in this source, a deflection of only $\sim 1^\circ$ is enough to increase the apparent speed of component J3 to that of component J2. In particular, from the theory of superluminal motion (Pearson & Zensus 1987) the minimum viewing angle θ_{min} goes from 2.60° to 1.54° if the apparent speed increases from $\beta_{app} = 22.0c$ (component J3) to $37.3c$ (component J2).

5. Conclusions and Summary

In this paper we carried out a multifrequency and multi-epoch study of PKS 1502+106 at VLBI resolution. The source morphology is highly variable and the jet structure is very complex on this scale.

We analyzed the structure of the jet, as seen in projection on the sky, and the changes in the position angle of the various jet components with the radial distance from the core. The results suggest that the jet components in PKS 1502+106 trace the same curved path. The jet undergoes two major bends, the first implies a change in the P.A. from $\sim 70^\circ$ to $\sim 110^\circ$ within 0.5 mas, while in the second bend the P.A. changes from $\sim 130^\circ$ to P.A. $\sim 80^\circ$ at 3–4 mas. Beyond that distance the VLBI jet points to the east at 7–15 mas.

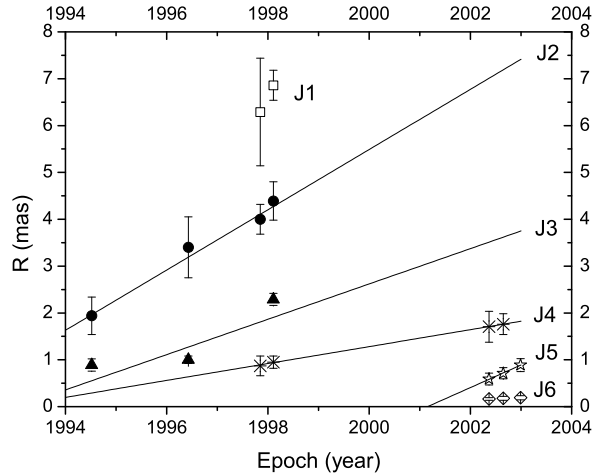


Fig. 8. Distances of the jet components from the core as a function of time. We included the data point at 5 GHz at epoch 1996.43 taken from Fomalont et al. (2000). All the other epochs are those presented in this paper. The line represents the linear fitting of the motion for each jet component.

Based on the model fitting results on the VLBI core, we obtain a weighted mean value of the Doppler factor, $\delta = 4.5 \pm 1.9$. The radio core brightness temperature in the source rest frame, $T_r = (2.0 \pm 0.5) \times 10^{11} K$, approaches the equipartition limit.

We detect superluminal motion in four components along the jet. The derived apparent speeds range between $10.5 \pm 2.6 c$ and $37.3 \pm 9.3 c$. Doppler boosting plays a major role in determining the observed properties of the source. In particular, the apparent speeds we derive suggest that the source is viewed under an angle to the line of sight $\theta < 5^\circ$, and that the bulk flow velocity is β_{intr} is $\sim 0.999 c$.

The ΔPA between the pc- and kpc-scale structure is about 30° , indicating that PKS 1502+106 belongs to the aligned population. The superluminal speeds in 1502+106 are much higher than the average value in radio loud quasars. We therefore conclude that PKS 1502+106 is more beamed than the overall population of radio loud quasars, and that its radio properties are more similar to the γ -ray loud quasars, although it is unclear if PKS 1502+106 is a γ -ray loud source to date. In particular, the superluminal speeds in this source are in the range found for the high redshift γ -ray loud quasars in other high frequency radio surveys (Jorstad et al. 2001).

A confirmation of γ -ray emission from this source would be highly valuable for our understanding of the γ -ray loudness phenomenon in radio loud quasars.

Acknowledgements. This research was supported by the National Science Foundation of PR China (10333020, 10328306 and 10373019), Foundation of Chinese Academy of Sciences (19973103). T. An thanks IRA of CNR for their hospitality during his visit to Italy for the data reduction in 2001. The studies reported in this paper have been supported by

the grant for collaborative research in radio astronomy of the CAS (Chinese Academies of Sciences) and CNR (the Italian National Research Council), Posiz. N. 132.20.1. This research has made use of the United States Naval Observatory (USNO) Radio Reference Frame Image Database (RRFID). The authors thank A.L. Fey for providing access to the RRFID datasets. The authors are also grateful to the staff of all EVN radio observatories and data reduction center, as well as the Hartebeesthoek observatory for support during the observations. The European VLBI Network is a joint facility of European, Chinese, South African and other radio astronomy institutes funded by their national research councils. This work has made use of NASA Astrophysics Data System Abstract Service.

References

Fey, A. L., Clegg, A. W., & Fomalont, E. B. 1996, *ApJS*, 105, 299

Fichtel, C.E., Bertsch, D.L., Chiang, J., et al. 1994, *ApJS*, 94, 551

Fomalont, E.B. 1999, in *Synthesis Imaging in Radio Astronomy II*, G.B. Taylor, C.L. Carilli, & R.A. Perley (eds.), P301

Fomalont, E.B., Frey, S., Paragi, Z., et al. 2000, *ApJS*, 131, 95

George, I.M., Nandra, K., Turner, T.J., et al. 1994, *ApJ*, 436L, 59

Güijosa, A., & Daly, R.A. 1996, *ApJ*, 461, 600

Hardee, P.E. 1987, *ApJ*, 318, 78

Hartman, R.C., Bertsch, D.L., Bloom, S.D., et al. 1999, *ApJS*, 123, 79

Hong, X.Y., Jiang, D.R., & Shen, Z.Q. 1998, *A&A*, 330, L45

Hong, X.Y., Wang, W.H., An, T., et al. 2004, in preparation

Impey, C.D., & Tapia S. 1988, *ApJ*, 333, 666

Jorstad, S.G., Marscher, A.P., & Mattox, J.R., et al. 2001, *ApJS*, 134, 181

Marscher A.P. 1987, in *Superluminal Radio Sources*, J.A. Zensus, & T.J. Pearson (eds.). Cambridge University Press, New York, P.208

Mattox, J.R., Schachter, J., Molnar, L., et al. 1997, *ApJ*, 481, 95

Murphy, D.W., Browne, I.W.A., & Perley, R.A. 1993, *MNRAS*, 264, 298

Pearson, T.J., & Zensus, J.A. 1987, in *Superluminal Radio Sources*, J.A. Zensus, T.J. & Pearson (eds.). Cambridge University Press, New Your, P. 1

Pearson, T.J., Browne, I.W.A., Henstock, D.R., et al. 1998, in *ASP Conf. Ser. 144, Radio Emission from Galactic and Extragalactic Compact Sources*, ed. J. A. Zensus, G. B. Taylor, & J. M. Wrobel (San Francisco: ASP), 17

Readhead, A.C.S. 1994, *ApJ*, 426, 51

Shen Z.Q., Wan, T.S., Moran, J.M., et al. 1997, *AJ*, 114, 1999

Shepherd, M.C., Pearson, T.J., & Taylor, G.B. 1994, *BAAS*, 26, 987

Tabara, H., & Inoue, M. 1980, *A&AS*, 39, 379

Thompson, D.J., Bertsch, D.L., Dingus, B.L., et al. 1995, *ApJS*, 101, 259

Zensus, J.A., Ros, E., Kellermann, K.I., et al. 2002, *AJ*, 124, 662